# The role of proton insertion in the charge storage behavior of the aqueous Zn/MnO$_2$ battery

Yifei Yuan[a,b,#], Ryan Sharpe[c,#], Kun He[a,b,*], Chenghang Li[a], Matthew Tamdoni Saray[b], Tongchao Liu[d], Wentao Yao[b], Meng Cheng[b], Huile Jin,[a] Shun Wang[a], Khalil Amine[d], Reza Shahbazian-Yassar[b*], M. Saiful Islam[c,e*], Jun Lu[d*]

[a] *College of Chemistry and Materials Engineering, Wenzhou University, Wenzhou 325035, China*

[b] *Mechanical and Industrial Engineering, University of Illinois at Chicago, Chicago, IL, 60607, USA*

[c] *Department of Chemistry, University of Bath, BA2 7AY, UK*

[d] *Chemical Sciences and Engineering Division, Argonne National Laboratory, Lemont, IL, 60439, USA*

[e] *Department of Materials, University of Oxford, Oxford OX1 3PH, UK*

** Corresponding authors: hekun@wzu.edu.cn; rsyassar@uic.edu;*
*saiful.islam@materials.ox.ac.uk; junlu@anl.gov*

[#] *Y.Y. and R.S. contributed equally to this work*

## Abstract

Amid the growing interest in rechargeable aqueous zinc-based batteries, tunnel-structured α-MnO$_2$ has emerged as a promising cathode material owing to its low cost, high capacity and high safety. However, the precise charge storage mechanism, possibly involving proton and/or Zn ion insertion, has not been fully characterized especially at the atomistic level. Here, we report new insights through a combined investigation of atomic-scale electron microscopy, electrochemical analysis and *ab initio* simulations. We find that reversible Zn$^{2+}$ insertion into α-MnO$_2$ framework is unlikely in the aqueous system, and that the charge storage process is dominated by H$^+$ insertion into the tunnel structures which are maintained upon discharging to HMnO$_2$. Furthermore, we identify the local lattice positions for the hydroxyl (OH) groups in H$_x$MnO$_2$ as a function of H content. We reveal the consequent anisotropic structural change proceeding from the particle surface into the bulk, and thus account for the structural failure and capacity decay of the electrode upon cycling. Future work should consider optimizing proton insertion kinetics with enhanced host stability.

# 1. Introduction

Aqueous Zn-metal-based rechargeable batteries are an emerging system for medium- to large-scale applications, including electric vehicles and load-levelling of intermittent power sources, due to their low cost, high safety and stable performance.[1,2,3,4,5] Various cathode materials have been tested to couple with the Zn anode, among which the $MnO_2$ system is particularly attractive owing to its easy processing, natural abundance and environmental advantages.[6,7,8,9] While the application of $MnO_2$ in primary (alkaline) batteries has been plagued by parasitic reactions, recent studies have significantly improved the rechargeability when immersed in a mild acidic aqueous electrolyte.[1,10,11,12]

There are intensive research efforts aimed at understanding the charge storage mechanisms of $\alpha$-$MnO_2$, which adopts a crystal structure based on an $MnO_6$ octahedral framework with one-dimensional 1×1 and 2×2 tunnels, allowing reversible insertion/extraction of charge carriers.[13,14,15,16] However, its precise charge storage mechanism as the cathode coupled with a Zn anode in aqueous mild acid electrolyte remains highly debated. Several mechanisms have been proposed: (1) $Zn^{2+}$ insertion into the tunnels whilst maintaining the original tunnel configuration[17]; (2) $Zn^{2+}$ insertion, resulting in the tunnel phase being converted to another phase, either spinel $ZnMn_2O_4$[18,19] or layered $Zn_xMnO_2$[20,21,22,23]; (3) $H^+$ insertion, with the tunnel phase converted to the hydrated phase (MnOOH);[1,24] or (4) co-insertion of both $Zn^{2+}$ and $H^+$ with the tunnel phase converted to MnOOH and $ZnMn_2O_4$.[2,25,26,27,28]

While many studies claim that the tunnel phase of $\alpha$-$MnO_2$ is completely changed to a new phase upon discharge and subsequently converted back to tunnels upon charge, we doubt such high structural reversibility under mild battery cycling conditions since our previous work on the tunnel formation mechanism points to a high demand for energy input and charge pre-ordering.[29] In addition, the conclusions drawn in previous studies[2,23] are mostly based on bulk-level characterizations such as x-ray diffraction (XRD) and energy dispersive spectroscopy (EDS), which detect signals at particle-assembly level; these approaches can be easily misinterpreted by the presence of side products or electrolyte residuals during sampling. It is thus important to elucidate the charge storage mechanism of this battery system by obtaining the precise composition, morphology and structure of single $MnO_2$ particles, preferably down to the atomic level. To the best of our knowledge, there is currently no such comprehensive microscopy study.

To fill this gap, we report a combined atomic level electron microscopy, electrochemistry and *ab initio* simulation study of the charge storage mechanism of the rechargeable aqueous $Zn/MnO_2$

battery system. Atomic structure imaging shows that the possibility of $Zn^{2+}$ intercalation into the $\alpha$-$MnO_2$ lattice is extremely low and that reversible $H^+$ intercalation into the tunnels is the dominant mechanism. In addition, the structural inhomogeneity within a single $MnO_2$ nanowire is revealed for the first time, showing that the tunnels on the surface region are severely distorted with a high degree of anisotropic expansion as a result of $H^+$ intercalation. *Ab initio* simulations of the structural and energetic changes on $H^+$ *vs* $Zn^{2+}$ insertion into the tunnel structures support our experimental observations as well as providing additional atomic insights, further advancing the fundamental understanding of the charge storage mechanism of this battery system.

## 2. Results and Discussion

### 2.1 Structural and battery performance analysis of $\alpha$-$MnO_2$ nanowires

The tunnels within as-synthesized $MnO_2$ nanowires are typically occupied by large cations such as $K^+$.[30] We therefore first investigated the effect of such cations on the performance of the $MnO_2$ cathode by removing $K^+$ from the tunnels using an acid-treatment method with the microscopic results shown in Figure 1a-c. Prior to the removal of tunnel cations, the presence of $K^+$ cations can be directly confirmed by combining EDS and atomic imaging, with their position clearly identified as the Wyckoff 2a site (Figure 1d). After the $K^+$ removal procedure, Figure 1a-c show no sign of $K^+$, indicating that $K^+$ has been successfully removed, leaving the tunnel space essentially empty and its framework well maintained. Note that the targeted $MnO_2$ sample in this work exhibits a nanowire-like morphology (Figure 1a) with [001] as the axis direction (also the tunnel direction). Figure 1b shows the [001] zone axis imaging of one shortened $\alpha$-$MnO_2$ nanowire piece (*i.e.* along the *c* direction, the same as the tunnel direction and the nanowire axial direction) after ultramicrotome sample preparation. Figure 1c shows the [010] zone axis imaging of $\alpha$-$MnO_2$ (*i.e.* along the *b* direction, the same as the nanowire radial direction). More crystallographic/imaging information of this sample is given in Supporting Information (SI) **Figure S1** (Supplementary Note 1).

The voltage profiles of the aqueous $Zn/MnO_2$ batteries with and without $K^+$ are given in SI **Figure S2**, where similar results are shown. Both profiles exhibit a single plateau between 1.2-1.3 V for the 1st discharge reaction, and two plateaus at 1.5 V and 1.6 V for the 1st charge reaction. For the subsequent cycles, the two-plateau phenomenon is reproducible for both charge (1.5 V and 1.6 V) and discharge (1.45 V and 1.3 V) reactions. The high consistency of the voltage profiles for $\alpha$-$MnO_2$ with and without $K^+$ points to a similar, if not identical, charge storage mechanism dominating these two scenarios. The stability of $K^+$ within the tunnels is relatively stable as further confirmed by *ex situ* STEM-EDS analyses (SI **Figure S3**), implying that the interaction between $K^+$ and inserted charge carriers is relatively weak. Based on this, we simplify the mechanism study in this work by focusing on α-$MnO_2$ without $K^+$ in the 2×2 tunnels.

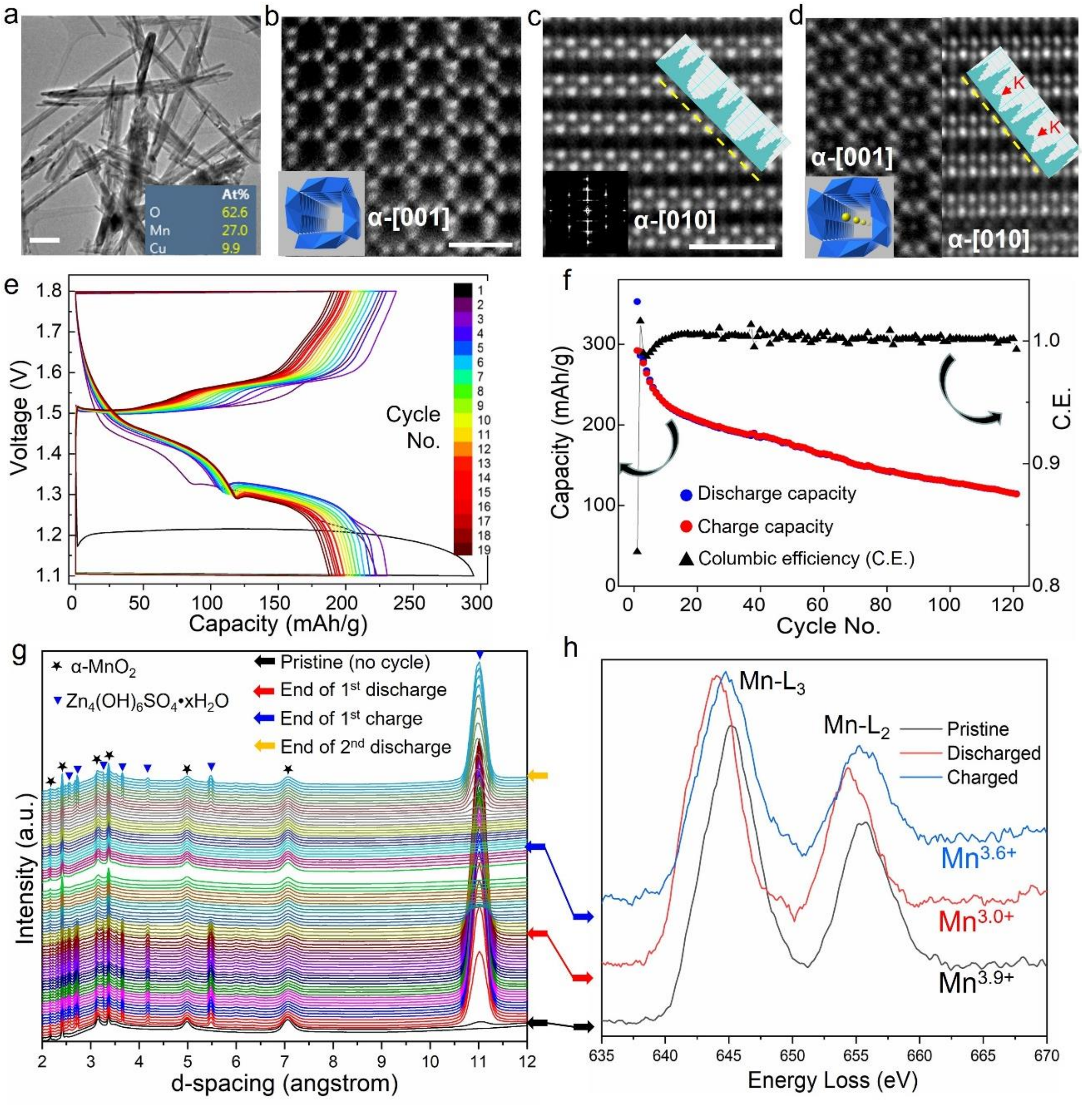

**Figure 1. Structure analysis and battery performance testing of α-$MnO_2$ nanowires.** (a) Low-mag TEM image showing the morphology of α-$MnO_2$ nanowires without $K^+$. Insets are the EDS quantification of associated elements. (b) [001] down-tunnel imaging (axial direction of the nanowire) showing the atomic structure of α-$MnO_2$ without $K^+$ occupying the tunnel center position. Each bright dot in the image represents an Mn atomic column. Insets are the corresponding polyhedral model. (c) [010] zone axis (radial direction of the nanowire) imaging showing the

atomic structure of α-$MnO_2$ tunnels without $K^+$ occupying the tunnel center position. Inset is the line profile depicting the intensity distribution in the region indicated by the yellow dashed lines. (d) [001] and [010] axes imaging showing the atomic structure of α-$MnO_2$ nanowires with $K^+$ occupying the tunnel center position. The red arrows in the line profile indicate the presence of a $K^+$ signal. Inset is the corresponding polyhedral model with $K^+$ ions (yellow dots) occupying the tunnel center (Wyckoff 2a site). Scale bars in (a) and (b-d) are 100 nm and 1 nm, respectively. (e) Voltage profiles of the first 19 cycles of a Zn/$MnO_2$ battery as a function of capacity. (f) The specific discharge/charge capacity (left Y axis) and the columbic efficiency (C.E., right Y axis) as a function of cycle number. (g) *In situ* XRD results showing the structural evolution of the α-$MnO_2$ electrode during the 1st cycle and the 2nd discharge process. (h) EELS analysis showing the valence change of Mn for the pristine, discharged and charged samples.

The focus on $K^+$-free α-$MnO_2$ facilitates the atomic scale analysis as discussed later; our aim to explore the possibility of $Zn^{2+}$ intercalation into the tunnel may have been compromised by the presence of $K^+$ in the tunnels, making the identification of possible $Zn^{2+}$ intercalation much more difficult. With this being said, the voltage profiles of an aqueous Zn/$MnO_2$ ($K^+$-free) battery are depicted in Figure 1e for its first 19 cycles. In addition to the aforementioned features of the profile, it is worth noting that with the increase of cycling number, the capacity contributed from the 1st discharge plateau (~1.45 V) and the 2nd discharge plateau (1.3 V) shows a reverse changing trend. The discharge capacity from the 1st plateau at ~1.45 V keeps increasing with cycling, while the one from the 2nd plateau at 1.3 V decreases with cycling in a more obvious fashion, resulting in an overall decreasing trend of the discharge capacity as a function of cycling number. This interesting phenomenon implies that the charge storage mechanisms for these two discharge plateaus are different.

In addition, we also measured the cycling performance of the α-$MnO_2$ electrode with the results given in Figure 1f. It shows that the first discharge capacity is above 300 mAh/g, very close to the theoretical capacity for this material assuming all Mn atoms are reduced to $Mn^{3+}$ as a result of charge carrier insertion. However, with increasing cycling number, both the discharge and charge capacity clearly decrease. After 120 cycles, the capacity of the $MnO_2$ electrode drops to ~100 mAh/g. The Columbic Efficiency, on the other hand, is roughly maintained at 100%, except for the first few cycles. This indicates that the capacity drop with cycling is caused by the irreversible structural change of the electrode material itself, which we will return to later. Decent long-term cycling performance of Zn-$MnO_2$ batteries at high rates has been reported previously[1,2,20,22]. We believe there are several key factors contributing to the reported high performance that are not implemented in our work, *e.g.* the use of $Mn^{2+}$ additives in the electrolyte, the phase or morphology control and surface engineering of $MnO_2$. All these strategies help to stabilize the structure of the $MnO_2$ host during high-rate cycling. In our work, with a main focus on investigating and understanding the charge storage mechanism in $MnO_2$, none of these performance-enhancing strategies are applied, and therefore the operational or failure mechanism of $MnO_2$ was more significant for us to target.

To further study the phase evolution of this system, *in situ* XRD was used to track the $MnO_2$ structure during cycling with the results shown in Figure 1g. It can be seen that the characteristic peaks of $\alpha$-$MnO_2$ remain strong and noticeable throughout the whole discharge-charge process, indicating that the tunnel phase is well maintained without obvious phase degradation caused by the reversible charge storage process. However, the $\alpha$-$MnO_2$ peaks exhibit slight broadening toward the larger d-spacing direction during discharge, possibly due to a strain or distortion effect as a result of charge storage. Some new and strong peaks immediately appear at d-spacings of 1.1 nm, 0.55 nm, and 0.42 nm at the beginning of the discharge process, whose intensity increases during discharge and decreases during charging. At the end of charge (to 1.8 V), these new peaks totally disappear. This phenomenon points to the existence of reversible phase formation/decomposition upon battery cycling, which should be different to the $MnO_2$-related structural evolution and will be later analyzed in detail combining the discussions of Figure 2.

It is also worth mentioning that the *in situ* XRD results fail to explain the difference in mechanism between the 1st and 2nd voltage plateaus within one discharge reaction, implying that kinetic factors may affect the battery reactions and should be further explored. To track the Mn valence change, electron energy loss spectroscopy (EELS) is used with the results presented in Figure 1h. Through comparison to previous work[31] and our quantification analyses, we find that during discharge, the Mn valence decreases from 3.9+ to 3.0+ and increases back to 3.6+ (rounded values) during the charge process, implying that the change of Mn valence as a result of charge storage is largely reversible due to the reversible insertion/extraction of cationic charge carriers. Refer to **SI Figure S4** and **Supplementary Note 1** for more details regarding Mn valence analysis.

## 2.2 Microscopy analysis of $H^+$ versus $Zn^{2+}$ insertion

The aforementioned XRD peak broadening and Mn valence change for the $\alpha$-$MnO_2$ electrode upon cycling indicates the existence of a reversible Faradaic charge storage reaction in single $\alpha$-$MnO_2$ particles. Intensive focus is thus put into the microscopic exploration of the $\alpha$-$MnO_2$ structure after discharge and its comparison with the scenario prior to discharge. Figure 2a-d show the STEM-EDS analysis for a single $MnO_2$ nanowire after the 1st discharge process. It can be seen in Figure 2a that the nanowire largely maintains the 1D shape with its surface unevenly covered by flake-like pieces. The EDS mapping in Figure 2b shows that while Mn and O reflect the shape of the $MnO_2$ nanowire, Zn seems to distribute within the flake-like pieces, not within the $MnO_2$ nanowire, indicating that the possibility of $Zn^{2+}$ insertion/intercalation into the $MnO_2$ lattice is very low. Furthermore, the compositional quantification shown in the insets of Figure 2a confirms that the nanowire is mainly composed of Mn and O (*i.e.* $MnO_2$) without the presence of Zn. Additional STEM-EDS analyses are provided for multiple sampling regions of the discharged $MnO_2$ nanowires as listed in the SI **Figure S5** (Supplementary Note 1), based on which we confidently state that $Zn^{2+}$ did not insert into the lattice of $MnO_2$. Instead, with the use of aqueous $ZnSO_4$ electrolyte (mild acidic, pH~4.8) in Zn/$MnO_2$ battery system, we suggest that the dominant charge storage mechanism is intercalation of $H^+$ ions into the $MnO_2$ tunnels without any phase transition.

The hypothesis of a proton intercalation mechanism is further tested by EDS analysis of the flake-like pieces generated during discharge in Figure 2a (inset), which are seen to be rich in Zn, O and S, with a Zn/S atomic ratio of ~4. Combined with the *in situ* XRD results in Figure 1g revealing emerging peaks at a d-spacing of 1.1 nm, one can reasonably claim these pieces to be $Zn_4(OH)_6SO_4 \cdot xH_2O$ (Zn/S atomic ratio is exactly 4) possessing a large layer spacing of ~1.1 nm supported by water molecules. The fact that this phase contains a large amount of $OH^-$ points to an $OH^-$-rich electrolyte as a result of $H^+$ insertion into the tunnels. Both the *in situ* XRD analysis (Figure 1g) and the *ex situ* TEM analysis (**SI Figure S6**) confirm that $Zn_4(OH)_6SO_4 \cdot xH_2O$ can be reversibly formed/decomposed during discharge/charge.

The lattice positions of the inserted protons as OH groups within the α-$MnO_2$ tunnels are addressed by *ab initio* modelling discussed below. It is worth mentioning that the previous studies supporting the theory of $Zn^{2+}$ insertion into $MnO_2$ generally relied on elemental analysis of the discharged $MnO_2$ electrode, either an EDS spectrum or elemental mapping;[2,23] however, we believe that these data sets could be misleading as such results cannot distinguish the Zn signals from the residual salts or other by-products (e.g. $Zn_4(OH)_6SO_4 \cdot xH_2O$ revealed in this work) that are adjacent or attached to the $MnO_2$ particles. Additional evidence excluding the possibility of $Zn^{2+}$ insertion into $MnO_2$ tunnels is provided by testing the performance of a Zn/$MnO_2$ batter using an aprotic electrolyte containing $Zn^{2+}$ salts, the result of which is given in **SI Figure S7**. Without $H^+$ in the electrolyte, the Zn/$MnO_2$ battery yields a limited capacity of 30 mAh/g at a current density of 50 mA/g, which corroborates the $H^+$-insertion driven charge storage mechanism in the aqueous Zn-$MnO_2$ battery system.

Another key evidence excluding the possibility of $Zn^{2+}$ insertion into $MnO_2$ tunnels is provided by atomic scale imaging of a single discharged $MnO_2$ nanowire along its two zone axes as shown in Figure 2c and d. The radially projected imaging in Figure 2c shows that the tunnels are essentially empty without the presence of Zn ions, as their occupation in the tunnels would have resulted in a brighter contrast in the line profile (inset in Figure 2c); indeed, the actual profile only shows the presence of Mn atomic columns. The tunnel structure is maintained after discharge as indicated by the fast Fourier transform (FFT) showing a typical $\alpha$-$MnO_2$-[010] zone axis pattern. This is further confirmed by directly imaging down the tunnels as shown in Figure 2d, where the 2×2 tunnel features of $\alpha$-$MnO_2$ are well maintained and the tunnels are essentially unoccupied by any heavy cations (such as $Zn^{2+}$ or $K^+$), leading to the conclusion that $H^+$ inserts into the $MnO_2$ lattice, whereas $Zn^{2+}$ does not. Note that the previous study of Pan *et al.*[1] has reported a seemingly similar mechanism of $H^+$-insertion in $\alpha$-$MnO_2$; a closer look, however, reveals significant differences in which they find that the discharge product of $MnO_2$ nanofibres to be much shorter MnOOH nanorods with completely different morphology and phase (denoted as $\alpha\text{-}MnO_2 + H^+ + e^- = MnOOH$). In contrast, our findings here point to a completely different mechanism featuring $H^+$-intercalation into $MnO_2$ with the original tunnel phase and nanowire morphology largely maintained (denoted as $\alpha\text{-}MnO_2 + H^+ + e^- = \alpha\text{-}H_1MnO_2$).

Figure 2e-h depicts the atomic analysis of one discharged $MnO_2$ nanowire along the tunnel direction. It is interesting to note that in Figure 2e the tunnel structures, although well maintained after discharge, exhibit non-uniform lattice distortion across the sampling region, particularly when comparing the tunnels close to the surface region with those in the bulk. Within the bulk of the nanowire, $MnO_2$ maintains its tetragonal symmetry without major distortion; in contrast, close to the surface region, obvious lattice distortion is captured and the tunnels in this region are severely distorted. Moreover, the distortion is seen to appear in an ordered fashion, *i.e.* the tunnels close to the surface are all distorted along one specific direction. This results in the increase of lattice parameter *a* and decrease of lattice parameter *b*, causing the deviation from the initial tetragonal symmetry (*a*-*b* angle ($\gamma$) reduces to 85°) as clearly illustrated in Figure 2e and h (and supported by atomistic modelling results detailed below). Such a change in symmetry is less obvious within the bulk region (*a*-*b* angle ($\gamma$) is 88°, close to 90°) though there is a similar *a*-increase and *b*-decrease trend as shown in Figure 2e and h depicting the intensity profiles of several unit cells along *a* and *b* directions.

We should note that there are a few studies reporting the direct microscopic imaging of hydrogen atoms in well-crystalized hydrides such as $YH_2$ and TiH[32,33]; achieving this goal in $MnO_2$ is, however, quite challenging due to several reasons. First, $H^+$ are electrochemically inserted into $MnO_2$ and can thus be considered as "foreign or dopant species" that distort the host lattice and thus largely compromises any effort toward direct $H^+$ imaging. Second, direct imaging of very small $H^+$ species requires the sample to be sufficiently thin (*e.g.* 8 nm for H imaging in $YH_2$ film-like sample[32]); however, it is technically challenging to thin one $MnO_2$ nanowire down to this level along its axis direction (down-tunnel imaging direction). Third, electrochemically inserted $H^+$ coordinated to oxygen has an O-H bond length of 0.10 nm as later discussed in the next section, which is quite close to the microscope's theoretical resolution (0.08 nm), disabling our trials of $H^+$ atomic imaging (without overlapping with O atomic columns).

It is worth mentioning that the effect of the electron beam on our observations can be ignored since $MnO_2$ materials are typically stable under normal TEM imaging conditions in comparison to other battery materials such as SEI and Li metal. The more severe distortion on the surface is not related to electron beam damage because first, the pristine $MnO_2$ material without $H^+$ insertion shows no sign of surface tunnel distortion under the same imaging conditions (see **SI Figure S1b** and related discussions), and second, the $H^+$-inserted tunnels show coordinated anisotropic distortion (*a*-increase and *b*-decrease), which cannot be caused by random electron beam damage. Moreover, such coordinated anisotropic lattice distortion implies that $H^+$ intercalation into the $MnO_2$ lattice follows an energetically favorable pathway, necessitating the implementation of *ab initio* modeling.

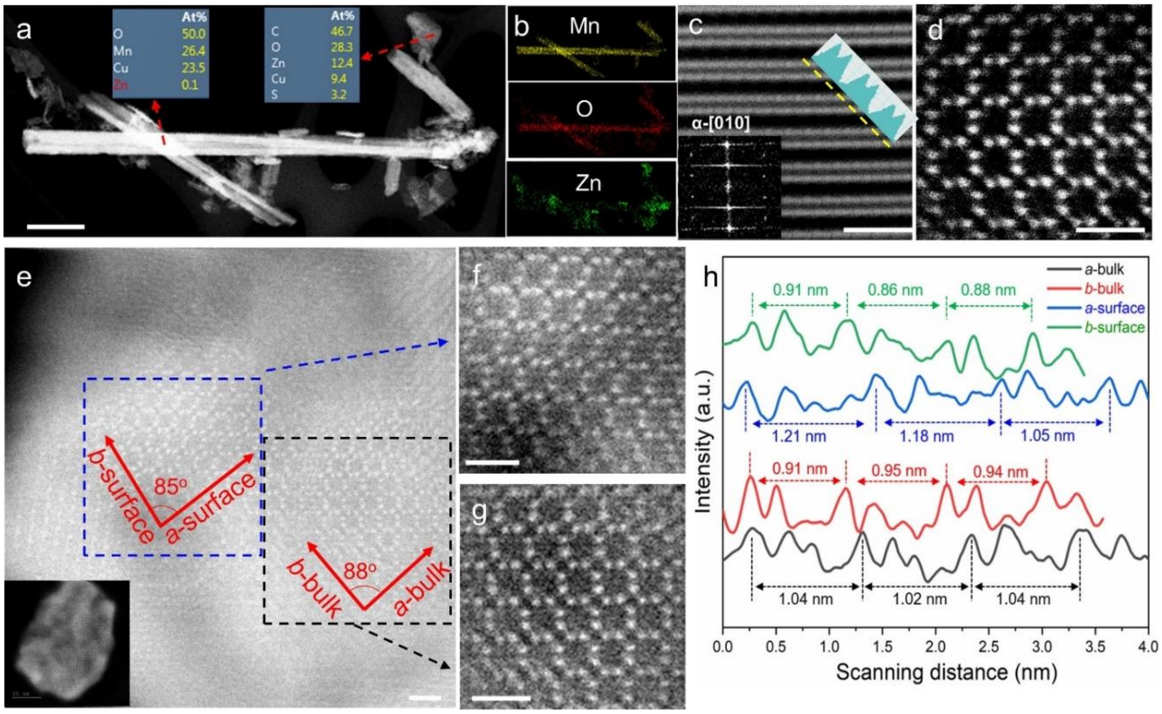

**Figure 2**. **STEM analysis of α-$MnO_2$ nanowires after discharge.** (a-d) High-angle annular dark field (HAADF)/EDS analysis of one $MnO_2$ nanowire after discharge, where (a) is the low-mag image of the nanowire featuring flake-like pieces adhered to its surface (insets are EDS-based compositional quantification from different locations as indicated by the red arrows), (b) is the STEM-EDS elemental mapping showing the distribution of Zn, Mn and O, (c, d) are the atomic scale [010] and [001] projections of $MnO_2$ demonstrating essentially "empty" tunnels without presence of large cations after discharge. (e-h) Down-tunnel STEM imaging (e-g) and line profiles (h) depicting the non-uniform and anisotropic tunnel distortion as a result of $H^+$ intercalation, where (f, g) are the atomic scale tunnel images captured from the surface region and the bulk region, respectively, and the line profiles are drawn exactly along the red arrows (also the *a-b* vector directions) indicated in (e). Scale bars in (a) and (c-g) are 100 nm and 1 nm, respectively.

## 2.3 Atomistic modeling insights into $H^+$ versus $Zn^{2+}$ insertion

We note that there are limited studies that have attempted to characterize the local structural positions or perturbations resulting from proton insertion in α-$MnO_2$, largely due to the difficulty in probing the exact positions of such tiny ions. To complement our microscopy work, we have therefore used *ab initio* simulations based on density functional theory (DFT) to examine the effect of proton and Zn ion insertion, and to identify the preferred proton (OH) positions in α-$H_xMnO_2$ (0

$\leq x \leq 1$) extending our previous computational work on $MnO_2$ materials.[34,35] (The computational methods including functionals and magnetic ordering are detailed in the Methods section and in the SI, Supplementary Note 2). We note that previous DFT studies[36,37] have examined $H^+$ insertion in other polymorphs of $MnO_2$ (such as γ- and β-$MnO_2$), but have not focused on both Zn and proton insertion in the Zn/α-$MnO_2$ system.

We first investigate the possible sites for proton insertion into the large 2×2 and small 1×1 tunnels of α-$H_xMnO_2$ by examining numerous configurations and their energetics at each composition (x). The lowest energy structures of α-$H_xMnO_2$ ($x$ = 0.25, 0.5, 0.75 and 1.0) are illustrated in Figure 3a-d, which show the positions and orientations of the OH groups formed by the inserted protons bonding to lattice oxygen ions. Two main features emerge. First, for compositions $0 < x \leq 0.5$ our results indicate that insertion adjacent to the trigonal pyramidal oxygen ion in the 2×2 tunnel has the lowest energy (Fig. 3a); the O-H bond length has a typical value of 1.0 Å. As might be expected, the calculations indicate that Mn is reduced from 4+ to 3+ as $H^+$ is inserted. Second, for $x > 0.5$, we find that insertion into the smaller 1×1 tunnel in addition to the 2×2 tunnel becomes favorable (Fig. 3c). The resulting structures indicate that the $H^+$ ions distribute as uniformly as possible to minimize the ion-ion electrostatic repulsion; for example, this feature is illustrated by the low energy structure of α-$H_{0.5}MnO_2$ containing two $H^+$ ions in each adjacent 2×2 tunnel (Fig. 3b). This result also accords with our previous DFT studies investigating Li-ion and Na-ion insertion sites and distribution in α-$MnO_2$.[38]

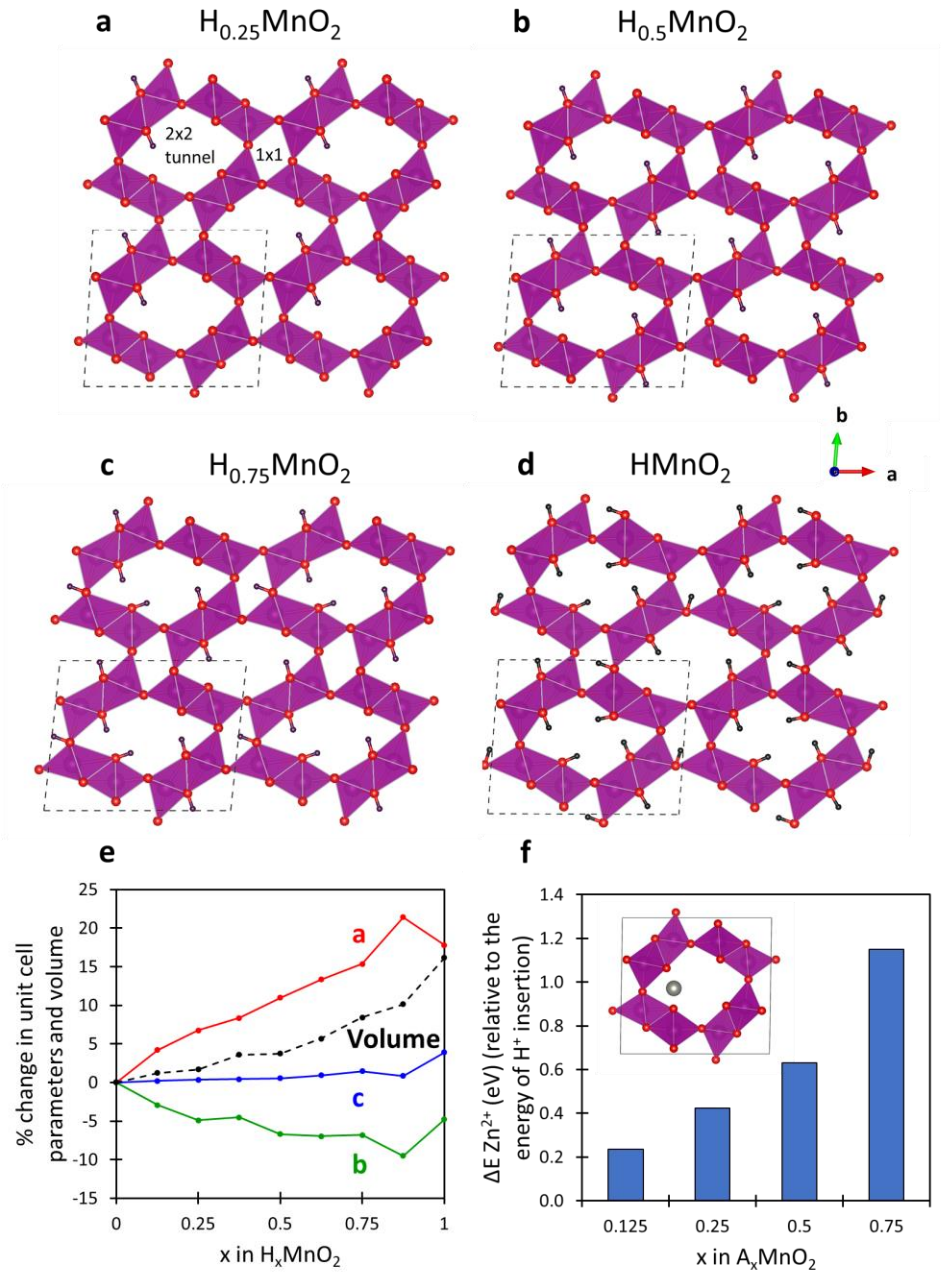

**Figure 3. Atomistic modeling insights into $H^+$ (versus $Zn^{2+}$) insertion.** (a)-(d) Lowest energy structures obtained for α-$H_xMnO_2$ (a) x=0.25, (b) x=0.5, (c) x=0.75, (d) x=1.0. Mn, O and H are shown by purple, red, and black, respectively. Representative unit cells are highlighted by dashed lines; for example, for $H_{0.25}MnO_2$ one H ion is in the central 2×2 tunnel and one H ion is in the top left 2×2 tunnel to give $H_2Mn_8O_{16}$ in total, or the stoichiometry $H_{0.25}MnO_2$. Structures for additional compositions x = 0.125, 0.375, 0.625, 0.875 are provided in the SI, **Figure S8**. (e) Calculated %

changes in the unit cell parameters (*a*, *b*, and *c*) and volume as $H^+$ is inserted into $H_xMnO_2$ ($0<x\leq1$). (f) Change in the energy of $Zn^{2+}$ insertion relative to the energy of $H^+$ insertion into $A_xMnO_2$, where x is 0.125, 0.25, 0.5 and 0.75, and A is $H^+$ or $Zn^{2+}$. Insertion energies for H and Zn into $MnO_2$ were calculated by comparing the energy of empty $MnO_2$ and an isolated H atom or Zn metal to the atom intercalated within $A_xMnO_2$ (A = H or Zn) as a function of x. Inset shows, as an example, the calculated lowest energy structure of $Zn_{0.125}MnO_2$.

The high levels of proton insertion are also important to structural changes. The variations in the calculated lattice parameters and unit cell volume of protonated α-$H_xMnO_2$ as a function of hydrogen content (x) are plotted in Figure 3e. It can be seen that the unit cell volume expands with increasing $H^+$ content, which is partly attributed to the increase of the effective ionic radii of the manganese cations on reduction from $Mn^{4+}$ (0.53 Å) to $Mn^{3+}$ (0.645 Å). The change in unit cell volume of protonated $H_xMnO_2$ structures exhibit a non-linear dependence, expanding by only +4% up to x=0.5, but by +16% at x = 1.0. This significant structural change from x = 0.5 and the aforementioned change of proton positions from 2×2 tunnels to 1×1 tunnels may be related to the two-plateau feature of the voltage profiles as shown in Figure 1e. It can then be reasonably proposed that the elongation of the 1st discharge plateau (~1.45 V) and the shortening of the 2nd discharge plateau (1.3 V) with increasing cycling number could be directly related to the change of $H^+$ insertion kinetics in 2×2 tunnels (for the 1st plateau) and 1×1 tunnels (for the 2nd plateau), respectively.

The diffusion coefficient of $H^+$ as a function of discharge capacity is experimentally measured to test this hypothesis with the results given in **SI Figure S9**. The 1st plateau exhibits improved $H^+$ insertion kinetics with a diffusion coefficient value in the range of $10^{-13}$-$10^{-12}$ $cm^2/s$, whereas the 2nd plateau exhibits much poorer $H^+$ insertion kinetics with a lower diffusion coefficient value in the range of $10^{-16}$-$10^{-14}$ $cm^2/s$. Therefore, the drastic shortening of the 2nd plateau during cycling should be ascribed to the poorer $H^+$ insertion kinetics in the 1×1 tunnels (during the 2nd plateau stage), which gradually degrades $MnO_2$ crystallinity and causes the overall capacity to decay as a function of cycling number. **SI Figure S10** further compares the cyclability of two $MnO_2$ electrodes when discharged to 1.1 V *vs* 1.32 V, where the electrode discharged to 1.32 V exhibits much better stability and capacity retention than the electrode discharged to 1.1 V during long-term cycling.

Regarding the crystal structure, the *ab initio* simulations also show that the lattice symmetry changes with the *a*-*b* angle (γ) decreasing from 90° to 88.5° on proton insertion to form $HMnO_2$, which is in very good agreement with the experimental atomic microscopy value of 88° in bulk $HMnO_2$ shown in Figure 2e. This result is highlighted in Figure 3e, showing the calculated increase of up to 20% in lattice parameter *a* and the corresponding decrease of up to 10% in lattice parameter *b*, also observed experimentally in our STEM analysis (Figure 2h). Hence, our atomistic simulations have helped to quantify the anisotropic tunnel structural change along the *a* and *b* directions and the consequent change in the tetragonal symmetry. From experiment, the lattice distortion is more obvious in the particle surface region probably due to the diffusion-controlled $H^+$ insertion kinetics. The DFT results also confirm that, despite the tunnel expansion and change in symmetry, the tunnels themselves remain well maintained and do not collapse upon proton intercalation. We note that *ab initio* molecular dynamics simulations of protonated $\alpha$-$MnO_2$ (detailed in the SI, Supplementary Note 2 and **Figure S11**) indicate that there is no fast or long-range proton conduction *via* hopping between oxygen sites.

In order to expand on our experimental work, we used DFT methods to further investigate whether $H^+$ or $Zn^{2+}$ insertion into $MnO_2$ is preferred. The approach used to identify the possible sites for $Zn^{2+}$ insertion is discussed in the SI (Supplementary Note 3 and **Figure S12**) and follows our previous studies investigating Li-ion and Na-ion insertion into $\alpha$-$MnO_2$.[38] Figure 3f shows the energy of $Zn^{2+}$ insertion into $Zn_xMnO_2$ as a function of Zn content (x), relative to the corresponding $H^+$ insertion energy. An important finding is that at low content ($x = 0.125$), $Zn^{2+}$ insertion is already unfavorable in comparison to proton insertion. As x increases, $Zn^{2+}$ insertion becomes increasingly energetically unfavorable. This result is in accord with our STEM analysis and other experimental studies[1,24] in which there is no evidence for $Zn^{2+}$ insertion.

As discussed in the Introduction, previous studies have also proposed a charge storage mechanism of co-insertion of $H^+$ and $Zn^{2+}$ into the $MnO_2$ lattice.[2,25,26] In order to probe the possibility that the two-step discharge plateau (Figure 1e) is caused by the insertion of $H^+$ and then $Zn^{2+}$, we investigated $Zn^{2+}$ insertion into $\alpha$-$H_{0.5}MnO_2$ using DFT. The most stable $Zn^{2+}$ insertion site was in the 1×1 tunnel (shown in Figure S5 in the SI), but this configuration was still found to be higher in energy (221 meV per formula unit) than inserting another proton into $\alpha$-$H_{0.5}MnO_2$. This indicates that, even after initial proton intercalation up to $H_{0.5}MnO_2$, $Zn^{2+}$ insertion remains unfavorable. In short, our combined experimental and computational results indicate that $H^+$ insertion is always more favorable than either $Zn^{2+}$ insertion or $Zn^{2+}/H^+$ co-insertion.

## 2.4 Mechanism for cycling-induced capacity decay

As $H^+$ intercalation/extraction continues for several cycles, the $MnO_2$ host will experience repetitive Mn valence change together with lattice distortion and recovery. A possible hypothesis is that the capacity decay of the $MnO_2$ cathode upon cycling could be caused by loss of active $MnO_2$

mass. As such, the structural morphology evolution as a function of cycle number is analyzed. The SEM images of the electrode (SI, Supplementary Note 4, **Figure S13**) show that while the nanowires are clearly seen in the pristine electrode prior to cycling, they can be hardly observed in the electrode after 100 cycles as a result of gradual loss of the active $MnO_2$ mass.

Figure 4 further explores the structural change of the electrode during cycling. One can tell that with the cycle number increasing, $MnO_2$ nanowires gradually decompose; after 100 cycles, the nanowire-like particles can hardly be seen. In addition, after 50 cycles, some tiny needle-like nanograins appear. It is noticeable that their diameter and length seem to be independent of cycle number while the number of nanograins keep increasing, making them a major component after 100 cycles as shown in Figure 4c and d. This trend is further corroborated in **SI Figure S14** analyzing diffraction patterns of $MnO_2$ electrodes as a function of cycling number. HRTEM and atomic STEM-HAADF analysis in Figure 4e and f demonstrate that these cycling-induced nanograins have a large interlayer spacing of ~1 nm and that within two adjacent layers lies another layer featuring lower contrast atoms. High-resolution STEM-EDS analysis in Figure 4g shows that these tiny nanograins are rich in Zn, Mn and O but poor in S, exhibiting a Zn/Mn ratio of ~3:2. This composition is repeatable as indicated by additional EDS analysis from multiple sampling locations shown in the **SI Figure S15**. The Zn/Mn-rich nature of these nanograins indicates that there cannot be any $Zn^{2+}$-inserted manganese oxides derived from the $MnO_2$ host; rather, they are some precipitated phases from the electrolyte when it is rich in $Zn^{2+}$ and $Mn^{2+}$ as a result of $Mn^{2+}$ dissolution during the discharge process.

The presence of $Mn^{2+}$ in these nanograins is further confirmed using EELS with the results and discussion given in **SI Figure S4c (in the green circles)**. The phase identification is, however, quite challenging due to the difficulty in finding a reference Zn-Mn-O phase with a Zn/Mn ratio of 3:2 and a large interlayer spacing of ~ 1 nm; moreover, the highly disordered structure (rich in dislocations as shown **Figure S16**) and the tiny-shaped nature of the nanograins disable any X-ray-based diffraction analysis at the bulk level. We thus provided more structural analyses of these nanograins under different zone axes in **SI Figure S17**, hopefully to facilitate future identification. It is worth mentioning that these cycling-induced nanograins seem to be irreversible. Once they are formed and attached to the electrode, they cannot be electrochemically decomposed during the charge process (see their presence after charge in **SI Figure S16**), which could be a key reason accounting for the capacity decay of the $MnO_2$ cathode after long-term cycling.

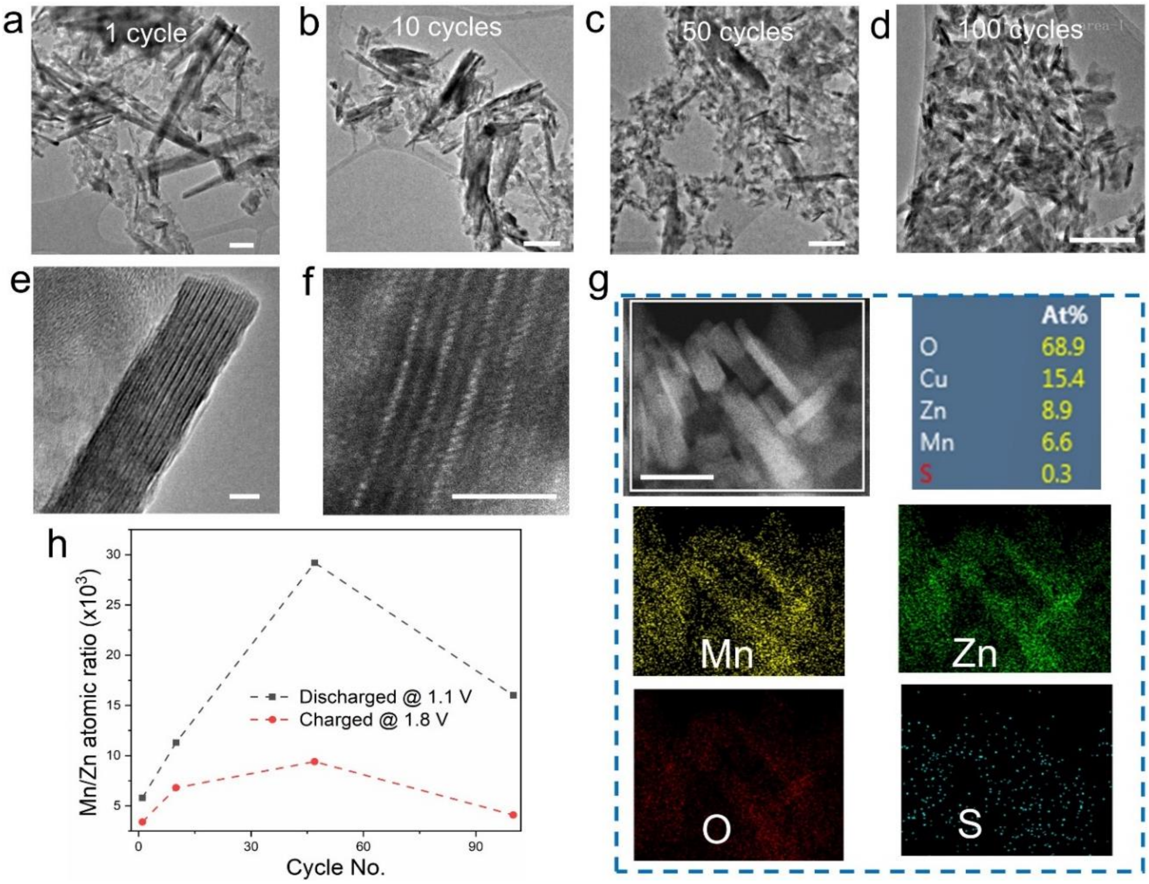

**Figure 4**. **Morphological and structural analysis of the α-$MnO_2$ electrode during long cycling conditions**. (a-d) Low-mag TEM images of the scratched sample from the $MnO_2$ electrode with different cycling numbers; (e-f) HRTEM and atomic STEM-HAADF images showing the layered structure of the tiny nanograins formed after cycles; (g) STEM-EDS analysis showing the compositional quantification of the tiny nanograins as well as the elemental distribution; (h) ICP-evaluated Mn/Zn atomic ratio in the electrolyte as a function of cycling number, where both discharged and charged electrolytes are analyzed. Scale bars in (a-d) are 100 nm, in (e,f) are 3 nm and in (g) are 50 nm.

To test the mechanism of $Mn^{2+}$ dissolution and irreversible Zn-Mn-O nanograin precipitation for capacity decay, Inductively Coupled Plasma (ICP) analysis of the electrolytes with different cycles is carried out. The Mn concentration in the electrolyte is evaluated with reference to the Zn concentration, with the latter considered to be relatively constant in the electrolyte reservoir. The Mn/Zn ratio in the electrolyte solutions collected after different cycles is shown in Figure 4h. It can be seen that within 50 cycles, the Mn concentration keeps increasing, indicating the gradual accumulation of dissolvable $Mn^{2+}$ in the electrolyte as a result of $H^+$ intercalation and $Mn^{3+}$

disproportionation reaction. For the charged electrolyte, the $Mn^{2+}$ concentration largely decreases but also exhibits a slight increasing trend with cycle number; this indicates that the $Mn^{3+}$ disproportionation reaction is largely but not totally reversible and that $MnO_2$ gradually loses its active mass after each cycle. After 50 cycles, however, for both the discharged and charged electrolyte, the Mn concentration has decreased with increasing cycle number, which points to the reprecipitation of $Mn^{2+}$ with the irreversible formation of tiny nanograins as discussed above.

## 3. Conclusions

The charge storage mechanism of the rechargeable aqueous Zn/α-$MnO_2$ battery system was investigated using a powerful combination of atomic-scale imaging, electrochemistry analysis and *ab initio* simulation techniques. From detailed analysis of the α-$MnO_2$ tunnel structures after cycling, the possibility of $Zn^{2+}$ insertion into the lattice is excluded and all findings lead to the conclusion that $H^+$ insertion dominates the charge storage process. Moreover, the tunnel framework is well maintained upon $H^+$ insertion up to $HMnO_2$. We have identified the $H^+$ insertion sites within the α-$MnO_2$ structure forming hydroxyl (OH) groups in the large 2×2 and smaller 1×1 tunnels, which maintains the tunnel structural integrity upon cycling. The significant structural change from $H_xMnO_2$ ($x = 0.5$) and the change of proton positions from 2×2 tunnels to 1×1 tunnels may be related to the observed two-plateau feature of the voltage profiles. High levels of $H^+$ insertion within α-$MnO_2$ tunnels results in anisotropic unit cell expansion, which significantly changes the original tetragonal symmetry of the host structure. After long-term cycling, this distortion leads to tunnel structural failure *via* Mn dissolution and irreversible reprecipitation into Zn-Mn-O nanograins with a Zn:Mn atomic ratio of 3:2.

Our systematic study provides valuable atomic-scale insights into the energy storage behavior of the α-$MnO_2$ electrode in the aqueous rechargeable Zn-metal-based battery, and points towards future design routes to improve the battery performance. Potential strategies include the suppression of Mn dissolution and the tuning of proton insertion kinetics within the tunnel framework of $MnO_{2.}$

## Methods

*Material synthesis*:

$\alpha$-$MnO_2$ nanowires are prepared by a hydrothermal reaction. $KMnO_4$ (0.9878 g) and $MnSO_4 \bullet H_2O$ (0.4226 g) are mixed in 80 mL deionized (DI) water to form a purple solution. The obtained slurry was then sealed into a 100 mL autoclave and heated at 160 $^oC$ for 12 hours. After centrifugation and DI water wash of the obtained products, a 4-day acid treatment using concentrated $HNO_3$ was applied to remove tunnel cations ($K^+$) as previously reported.[39] Then, the nanowires were washed by DI water several times until the pH value of the solution is ~7.

### *Materials characterizations:*

*In-situ high-energy X-ray diffraction (HEXRD)*: HEXRD was performed at the 11-ID-C beamline of the Advanced Photon Source at Argonne National Laboratory. A high-energy X-ray with a beam size of 0.2 mm×0.2 mm and wavelength of 0.1173 Å was used. Diffraction patterns were collected in the Laue diffraction geometry using a Perkin-Elmer area detector, placed at 1800 mm from the samples. The high penetration and low absorption of HEXRD is beneficial to observe tiny phase changes that are usually invisible from lab scale XRD. The 2032-coin cells have a 3 mm hole suitable for X-rays to pass through and diffraction patterns were collected every 10 minutes. Kapton tape was used to seal the holes of the coin cells, preventing them from air exposure.

*Microscopic analysis*: The cross-sectioned $MnO_2$ sample for down-tunnel imaging was prepared via ultramicrotome with a diamond knife and a cutting step size of 200 nm. The embedding of the nanowires was done using epoxy resin and hardener. The TEM/STEM data were obtained using an aberration corrected JEOL ARM 200CF microscope with a 200 kV gun and a 22 mrad convergence angle. EDS data were acquired using an Oxford X-Max 100TLE windowless SDD. EELS data were obtained using a Gatan GIF Continuum (5 mm entrance aperture, dual-EELS mode, ~53 mrad collection angle). The energy dispersion was set to be 0.2 eV/channel. A ~0.8 eV full-width at half maximum of zero loss peak was measured to be considered as the energy resolution (see **SI Figure S4a**), which can be considered as a moderate energy resolution and it should have limited effect on Mn valence quantification based on peak area integration since the same analysis method is consistently applied to all samples of interest in this work. The background was subtracted using the Power Law mode by placing a ~50 eV window right before the white line peak onset positions to define the background (see **SI Figure S4b**). The spectra were fitted using a Gaussian function with a R-square value >0.99. The quantification of Mn valence is carried out using two independent methods: one is the Mn $L_3/L_2$ edge white line ratio ($I(L_3/L_2)$) method and the other one is the energy difference between Mn $L_3$ and $L_2$ ($\Delta E(L_2$-$L_3)$). See **Supplementary Note 1** for more information.

*Electrochemical testing*: The $MnO_2$ cathode for battery testing is made of 10 wt% polyvinylidene difluoride binder in N-methyl-pyrrolidinone, 10 wt% super P carbon and 80 wt% a-MnO2. The mixture was then cast onto stainless steel foils to make the electrode. The electrode was dried at 70 $^oC$ for 4 h, followed by thorough drying at 70 $^oC$ overnight under vacuum. Battery testing was carried out using CR2032 coin cells with Zinc metal as the counter electrode, 1 M $ZnSO_4$ aqueous solution as the electrolyte, and glass microfiber as the separator. Cells were cycled between 1.8 and 1.0 V. Prior to the battery cycling, the cross-sectioned $MnO_2$ sample was preloaded to a TEM grid, which was then placed adjacent to the $MnO_2$ electrode laminate and got cycled with the electrode simultaneously until intentionally terminated for *ex situ* TEM analysis. GITT was tested using the following procedure: The lamination of the $MnO_2$ electrode and battery assembly operations are the same as that for the normal battery performance testing. After 2 normal discharge-charge cycles (30 mA/g between 1.8 V and 1.1 V), the 3rd discharge process was targeted for the GITT measurement. The discharge current was set at 15 mA/g and it ran for 30 min every time with an intermittent rest period of 3 hours. This procedure was repeated until the discharge voltage is dropped below 1.1 V.

*ICP measurement*: ICP was done using an ICP spectrometer (iCAP 7000 Series). The sample was directly obtained by collecting the electrolytes of cycled Zn/$MnO_2$ coin cells after they were opened in atmosphere.

## *Computational methods*:

Computational methods based on density functional theory (DFT) are well established for examining properties of battery electrode materials.[40,41,42,43] All calculations here were performed using periodic DFT as implemented in the Vienna ab-initio simulation package (VASP).[44,45,46] A plane-wave basis set to represent the wavefunctions and the projected augmented wave (PAW) method were used.[47,48] The exchange-correlation energy was calculated within the generalized gradient approximation using the Perde–Burke–Ernzerhof functional.[49] A planewave cut-off of 520 eV and a minimum of 6×6×20 k-points were used for each calculation. As in previous work,[38] the calculations were performed in a ferromagnetic spin polarized configuration and using the DFT+U approach[50] in order to account for on-site Coulomb interactions. A U - J value of 5.2 eV and a J value of 1.0 eV was used for Mn, as determined in previous work.[38] The ionic and electronic self-consistent convergence was set to $5\times10^{-2}$ and $1\times10^{-5}$ eV, respectively. We performed total energy calculations in a 1×1×1 cell (24 atoms) of $\alpha$-$MnO_2$ using the experimental structure[51] at room temperature. The $\alpha$-$MnO_2$ crystal occurs in the tetragonal space group I4/m (no. 87) with lattice parameters $a = b = 9.815$ Å and $c = 2.847$ Å. In Table S3 we show the calculated lattice parameters for α-$MnO_2$, which agree with the experimental parameters to within 3.2%. Ewald energies were used to screen for candidate low energy configurations of $Zn_xMnO_2$, where x = 0.5 and 0.75, due to the huge number of possible configurations. These low energy candidates were then treated with *ab initio* DFT which more fully describes the electronic effects of the system. Well-established methodology has been used in previous computational studies of battery materials to calculate ion insertion (intercalation) energies [38,52]. Likewise, insertion energies for H and Zn into $MnO_2$ were calculated by comparing the energy of empty $MnO_2$ and an isolated H atom or Zn metal to the atom intercalated within $MnO_2$ using the most favorable ion sites. As well as ferromagnetic ordering, we performed test proton insertion calculations on $H_{0.125}MnO_2$ with antiferromagnetic ordering, which produced the same energetic trends and lowest energy ion sites. We recognize that there is significant debate in the existing literature on the magnetic ordering in α-$MnO_2$ which we detail in **SI Note 2**. Our DFT calculations find ferromagnetic ordering only slightly more favorable than antiferromagnetic ordering. We stress that magnetic behavior was not our focus here and our simulations have provided valuable atomic-scale insights and energetic trends into $Zn^{2+}$ insertion *versus* $H^+$ insertion in the charge storage process.

## Acknowledgements

This work was financially supported by the Natural Science Foundation of China (Grant No. 52002287). R. Shahbazian-Yassar is thankful to National Science Foundation (NSF) Award CBET-1805938. RS and MSI thank the EPSRC (LiBatt programme grant EP/M0009521/1) and the Faraday Institution (CATMAT project FIRG016, FIRG035) for financial support, and the HEC Materials Chemistry Consortium (EP/R029431), the Isambard HPC (EP/P020224/1) and the Balena HPC service (Bath) for supercomputer facilities. RS and MSI gratefully acknowledge useful discussions with Dr Pezhman Zarabadi-Poor (Oxford), Dr Lucy Morgan (Bath), Dr Kit McColl (Bath), Dr Matt J. Clarke (Bath), and Dr James Dawson (Newcastle). Work at Argonne National Laboratory was supported by the U. S. Department of Energy (DOE), Office of Energy Efficiency and Renewable Energy, Vehicle Technologies Office. Argonne National Laboratory is operated for DOE Office of Science by UChicago Argonne, LLC, under contract number DE-AC02-06CH11357. Use of the Advanced Photon Source (APS) {Beamline 9-BM} at Argonne National Laboratory, Office of Science user facility, was supported by the U. S. Department of Energy, Office of Science, Office of Basic Energy Sciences, under Contract No. DE-AC02-06CH11357. This work made use of instruments in the Electron Microscopy Service (Research Resources Center, UIC). We acknowledge Quantitative Bio-element Imaging Center (QBIC) at Northwestern University (US) for assistance of ICP measurement. We acknowledge Thermo Fisher Scientific's Shanghai Nanoport, particularly Dr. Suya Liu, for their consultative help in atomic imaging of light atoms using electron microscopy.

## References:

1. Pan, H. et al. Reversible aqueous zinc/manganese oxide energy storage from conversion reactions. *Nat. Energy* **1**, 16039 (2016).
2. Sun, W. et al. Zn/$MnO_2$ battery chemistry with $H^+$ and $Zn^{2+}$ coinsertion. *J. Am. Chem. Soc.* **139**, 9775-9778 (2017).
3. Blanc, L.E., Kundu, D. & Nazar, L.F. Scientific challenges for the implementation of Zn-ion batteries. *Joule* **4**, 771-799 (2020).
4. Wang, F. et al. Highly reversible zinc metal anode for aqueous batteries. *Nat. Mater.* **17**, 543-549 (2018).
5. Wang, X. et al. Advances and Perspectives of Cathode Storage Chemistry in Aqueous Zinc-Ion Batteries. *ACS Nano* **15***, 9244-9272* (2021).
6. Wu, D. et al. Quantitative temporally and spatially resolved X-ray fluorescence microprobe characterization of the manganese dissolution-deposition mechanism in aqueous Zn/α-$MnO_2$ batteries. *Energy Environ. Sci.* **13**, 4322-4333 (2020).
7. Chao, D. et al. An electrolytic Zn–$MnO_2$ battery for high-voltage and scalable energy storage. *Angew. Chem., Int. Ed.* **58**, 7823-7828 (2019).
8. Mateos, M., Makivic, N., Kim, Y.S., Limoges, B. & Balland, V. Accessing the two-electron charge storage capacity of $MnO_2$ in mild aqueous electrolytes. *Adv. Energy Mater.* **10**, 2000332 (2020).
9. Zhao, Q. et al. Proton Insertion Promoted a Polyfurfural/$MnO_2$ Nanocomposite Cathode for a Rechargeable Aqueous Zn–$MnO_2$ Battery. *ACS Appl. Mater. Interfaces* **12**, 36072-36081 (2020).
10. Mathew, V. et al. Manganese and vanadium oxide cathodes for aqueous rechargeable zinc-ion batteries: A focused view on performance, mechanism, and developments. *ACS Energy Lett.* **5**, 2376-2400 (2020).
11. Jiao, Y. et al. Enabling stable $MnO_2$ matrix for aqueous zinc-ion battery cathodes. *J. Mater. Chem. A* **8**, 22075-22082 (2020).
12. Zhu, X. et al. Superior-Performance Aqueous Zinc-Ion Batteries Based on the In Situ Growth of $MnO_2$ Nanosheets on $V_2CTX$ MXene. *ACS Nano* **15**, 2971-2983 (2021).
13. Yuan, Y. et al. Ordering heterogeneity of [$MnO_6$] octahedra in tunnel-structured $MnO_2$ and its influence on ion storage. *Joule* **3**, 471-484 (2019).
14. Yuan, Y. et al. Dynamic study of (De) sodiation in alpha-$MnO_2$ nanowires. *Nano Energy* **19**, 382-390 (2016).
15. Yuan, Y. et al. Revealing the Atomic Structures of Exposed Lateral Surfaces for Polymorphic Manganese Dioxide Nanowires. *Small Struct.* **2**, 2000091 (2021).
16. Lindberg, S. et al. Charge storage mechanism of α-$MnO_2$ in protic and aprotic ionic liquid electrolytes. *J. Power Sources* **460**, 228111 (2020).

17. Alfaruqi, M.H. et al. Enhanced reversible divalent zinc storage in a structurally stable α-$MnO_2$ nanorod electrode. *Journal of Power Sources* **288**, 320-327 (2015).
18. Alfaruqi, M.H. et al. A high surface area tunnel-type α-$MnO_2$ nanorod cathode by a simple solvent-free synthesis for rechargeable aqueous zinc-ion batteries. *Chem. Phys. Lett.* **650**, 64-68 (2016).
19. Xu, D. et al. Preparation and characterization of $MnO_2$/acid-treated CNT nanocomposites for energy storage with zinc ions. *Electrochim. Acta* **133**, 254-261 (2014).
20. Wu, B. et al. Graphene scroll-coated α-$MnO_2$ nanowires as high-performance cathode materials for aqueous Zn-ion battery. *Small* **14**, 1703850 (2018).
21. Lee, B. et al. Elucidating the intercalation mechanism of zinc ions into α-$MnO_2$ for rechargeable zinc batteries. *Chem. Commun.* **51**, 9265-9268 (2015).
22. Zhang, N. et al. Rechargeable aqueous zinc-manganese dioxide batteries with high energy and power densities. *Nat. Commun.* **8**, 405 (2017).
23. Lee, B. et al. Electrochemically-induced reversible transition from the tunneled to layered polymorphs of manganese dioxide. *Sci. Rep.* **4**, 6066 (2014).
24. Yang, J. et al. Unravelling the Mechanism of Rechargeable Aqueous Zn–$MnO_2$ Batteries: Implementation of Charging Process by Electrodeposition of $MnO_2$. *ChemSusChem* **13**, 4103 (2020).
25. Wang, J. et al. Superfine $MnO_2$ Nanowires with Rich Defects Toward Boosted Zinc Ion Storage Performance. *ACS Appl. Mater. & Interfaces* **12**, 34949-34958 (2020).
26. Li, Y. et al. Reaction mechanisms for long-life rechargeable Zn/$MnO_2$ batteries. *Chem. Mater.* **31**, 2036-2047 (2019).
27. Gao, X. et al. $H^+$-Insertion Boosted α-$MnO_2$ for an Aqueous Zn-Ion Battery. *Small* **16**, 1905842 (2020).
28. Huang, Y. et al. Novel insights into energy storage mechanism of aqueous rechargeable Zn/$MnO_2$ batteries with participation of $Mn^{2+}$. *Nano-Micro Lett.* **11**, 46 (2019).
29. Yuan, Y. et al. Deciphering the Atomic Patterns Leading to $MnO_2$ Polymorphism. *Chem* **5**, 1793-1805 (2019).
30. Yuan, Y. et al. Asynchronous crystal cell expansion during lithiation of $K^+$-stabilized α-$MnO_2$. *Nano Lett.* **15**, 2998-3007 (2015).
31. Tan, H., Verbeeck, J., Abakumov, A. & Van Tendeloo, G. Oxidation state and chemical shift investigation in transition metal oxides by EELS. *Ultramicroscopy* **116**, 24-33 (2012).
32. Ishikawa, R. et al. Direct imaging of hydrogen-atom columns in a crystal by annular bright-field electron microscopy. *Nat. Mater.* **10**, 278-281 (2011).
33. de Graaf, S., Momand, J., Mitterbauer, C., Lazar, S. & Kooi, B.J. Resolving hydrogen atoms at metal-metal hydride interfaces. *Sci. Adv.* **6**, eaay4312 (2020).
34. Tompsett, D.A., Parker, S.C. & Islam, M.S. Rutile (β-) $MnO_2$ surfaces and vacancy formation for high electrochemical and catalytic performance. *J. Am. Chem. Soc.* **136**, 1418-1426 (2014).
35. Tompsett, D.A., Parker, S.C., Bruce, P.G. & Islam, M.S. Nanostructuring of β-$MnO_2$: The important role of surface to bulk ion migration. *Chem. Mater.* **25**, 536-541 (2013).
36. Vasiliev, I., Magar, B.A., Duay, J., Lambert, T.N. & Chalamala, B. Ab initio studies of hydrogen ion insertion into β-, R-, and γ-$MnO_2$ polymorphs and the implications for shallow-cycled rechargeable Zn/$MnO_2$ batteries. *J. Electrochem. Soc.* **165**, A3517 (2018).
37. Balachandran, D., Morgan, D. & Ceder, G. First principles study of H-insertion in $MnO_2$. *J. Solid State Chem.* **166**, 91-103 (2002).

38. Tompsett, D.A. & Islam, M.S. Electrochemistry of hollandite α-$MnO_2$: Li-ion and Na-ion insertion and $Li_2O$ incorporation. *Chem. Mater.* **25**, 2515-2526 (2013).
39. Yuan, Y. et al. The influence of large cations on the electrochemical properties of tunnel-structured metal oxides. *Nat. Commun.* **7**, 13374 (2016).
40. Sharpe, R. et al. Redox Chemistry and the Role of Trapped Molecular $O_2$ in Li-Rich Disordered Rocksalt Oxyfluoride Cathodes. *J. Am. Chem. Soc.* **142**, 21799–21809 (2020).
41. Naylor, A.J. et al. Depth-dependent oxygen redox activity in lithium-rich layered oxide cathodes. *J. Mater. Chem. A* **7**, 25355-25368 (2019).
42. Li, Y. et al. Fluid-enhanced surface diffusion controls intraparticle phase transformations. *Nat. Mater.* **17**, 915-922 (2018).
43. Tapia-Ruiz, N. et al. High voltage structural evolution and enhanced Na-ion diffusion in P2-$Na_{2/3}Ni_{1/3-x}Mg_xMn_{2/3}O_2$ ($0 \leqslant x \leqslant 0.2$) cathodes from diffraction, electrochemical and ab initio studies. *Energy Environ. Sci.* **11**, 1470-1479 (2018).
44. Kresse, G. & Furthmüller, J. Efficient iterative schemes for ab initio total-energy calculations using a plane-wave basis set. *Phys. Rev. B* **54**, 11169 (1996).
45. Kresse, G. & Hafner, J. Ab initio molecular dynamics for liquid metals. *Phys. Rev. B* **47**, 558 (1993).
46. Kresse, G. & Hafner, J. Ab initio molecular-dynamics simulation of the liquid-metal–amorphous-semiconductor transition in germanium. *Phys. Rev. B* **49**, 14251 (1994).
47. Blöchl, P.E. Projector augmented-wave method. *Phys. Rev. B* **50**, 17953 (1994).
48. Kresse, G. & Joubert, D. From ultrasoft pseudopotentials to the projector augmented-wave method. *Phys. Rev. B* **59**, 1758 (1999).
49. Perdew, J.P., Burke, K. & Ernzerhof, M. Generalized gradient approximation made simple. *Phys. Rev. Lett.* **77**, 3865 (1996).
50. Dudarev, S., Botton, G., Savrasov, S., Humphreys, C. & Sutton, A. Electron-energy-loss spectra and the structural stability of nickel oxide: An LSDA+ U study. *Phys. Rev. B* **57**, 1505 (1998).
51. Kondrashev, Y.D. & Zaslavskii, A. The structure of the modifications of manganese (IV) oxide. *Izvestiya Akademii Nauk SSSR, Seriya Fizicheskaya* **15**, 179-186 (1951).

52. Islam, M.S. & Fisher, C.A.J. Lithium and sodium battery cathode materials: computational insights into voltage, diffusion and nanostructural properties. *Chem. Soc. Rev.* **43**, 185-204 (2014).